



Overdense Threads in the Solar Corona Induced by Torsional Alfvén Waves

Sergio Díaz-Suárez^{1,2} and Roberto Soler^{1,2} ¹ Departament de Física, Universitat de les Illes Balears, E-07122, Palma de Mallorca, Spain; s.diaz@uib.es² Institute of Applied Computing & Community Code, Universitat de les Illes Balears, E-07122, Palma de Mallorca, Spain

Received 2021 October 22; revised 2021 November 12; accepted 2021 November 15; published 2021 November 25

Abstract

High-resolution and high-cadence observations have shown that Alfvén waves are ubiquitous in the solar atmosphere. Theoretical works suggest their ability to transfer large energy fluxes from the photosphere to the corona and solar wind. In this proof-of-concept Letter we show that torsional Alfvén waves can induce the formation of filamentary plasma structures in the solar corona. We perform high-resolution 3D ideal MHD simulations in an initially uniform coronal plasma permeated by a line-tied twisted magnetic field. We find that torsional Alfvén waves develop Kelvin–Helmholtz instabilities as a result of the phase mixing process. The Kelvin–Helmholtz instability drives plasma compression that breaks the uniformity of density, creating elongated overdense threads aligned with the direction of the magnetic field. With synthetic modeling of SDO/AIA imaging we show that the overdense filaments could be seen in observations as fine strands that illuminate the underlying magnetic structure.

Unified Astronomy Thesaurus concepts: [Alfven waves \(23\)](#); [Magnetohydrodynamical simulations \(1966\)](#); [Solar physics \(1476\)](#); [Solar corona \(1483\)](#)

Supporting material: animations

1. Introduction

Alfvén waves are magnetohydrodynamic (MHD) waves whose restoring force is magnetic tension (Alfvén 1942). They are polarized transversely to the magnetic field direction and are nearly incompressible. Torsional Alfvén waves (TAW) are a subclass of axisymmetric waves that drive periodic twisting (torsion) of the magnetic field lines (see, e.g., Spruit 1982). In the solar atmosphere, TAW have been detected in photospheric bright points (Jess et al. 2009), chromospheric spicules (De Pontieu et al. 2012), during solar flares (Aschwanden & Wang 2020), and in coronal structures (Kohutova et al. 2020). Theoretical works suggest that TAW are able to transport large energy fluxes from the photosphere to the corona and solar wind despite the strong chromospheric filtering (e.g., Soler et al. 2019, 2021).

In the presence of a continuous spectrum, TAW undergo the process of phase mixing and develop shear flows that can trigger the Kelvin–Helmholtz instability (KHi; see Heyvaerts & Priest 1983; Browning & Priest 1984). In coronal loops, the nonlinear evolution of this process leads to turbulence (Díaz-Suárez & Soler 2021). Similar results were previously obtained in the case of kink MHD waves (see, e.g., Terradas et al. 2008; Antolin et al. 2014; Magyar & Van Doorsselaere 2016; Howson et al. 2017; Karamelas et al. 2017; Pagano et al. 2020, among other efforts). However, unlike kink MHD waves, TAW do not require a preexisting tube or density enhancement that acts as an established waveguide. Therefore, TAW can be considered as a more fundamental type of oscillation of the magnetic field.

This Letter is a proof-of-concept work whose purpose is to demonstrate that the nonlinear evolution of TAW can induce

the spontaneous formation of filamentary structures in the solar coronal medium. The process relies on the excitation of the KHi via phase mixing shear flows and does not need the presence of a preexisting density enhancement. The KHi drives plasma compression in the form of elongated threads locally aligned with the direction of the magnetic field. To illustrate the fundamentals of this mechanism, we consider the paradigmatic scenario of a twisted magnetic field embedded in a uniform plasma. The evolution of standing TAW and the associated formation of overdense threads are studied with MHD numerical simulations, while synthetic modeling of extreme ultraviolet (EUV) emission is used to discuss possible observational signatures of the process.

2. Initial Configuration and Numerical Setup

In this numerical experiment, we aim to represent with a simple model the solar coronal plasma permeated by a twisted magnetic field. We assume a uniform background density, $\rho = \rho_0$. Gravity is neglected. For the magnetic field, we consider the uniform twist model adapted from Gold & Hoyle (1960), namely

$$B_r = 0, \quad (1)$$

$$B_\varphi = \frac{cB_0 r/R}{1 + c^2(r/R)^2}, \quad (2)$$

$$B_z = \frac{B_0}{1 + c^2(r/R)^2}, \quad (3)$$

with B_r , B_φ , and B_z the magnetic field components in a cylindrical coordinate system (r, φ, z) . B_0 is the magnetic field strength at $r=0$, R is the radial length scale, and c is a parameter that controls the amount of twist. The magnetic field is invariant in the azimuthal, φ , and longitudinal, z , directions. Since the magnetic field is force-free, we consider a uniform gas pressure, $p = p_0$, whose value is set so that the plasma β at

$r=0$ is $\beta_0 = \frac{\rho_0}{B_0^2/2\mu} = 0.2$. Therefore, the simulations are conducted in a low- β scenario.

The Cartesian computational box extends from $-3R$ to $3R$ in the x - and y -directions and from $-L/2$ to $L/2$ in the z -direction, with $L = 10R$. The magnetic field is assumed to be anchored (line-tied) at the bottom, $z = -L/2$, and top, $z = L/2$, boundaries, which represent the base of the corona. Hood & Priest (1979) studied the kink instability of the uniform twist model considering line-tying of the field lines and found that the maximum twist expressed with their parameter $\Phi = LB_\varphi/rB_z$ is $\Phi_{\text{crit.}} \approx 3.3\pi$. Their twist parameter Φ is related to our twist parameter by $c = \Phi R/L$, so that the critical value is $c_{\text{crit.}} \approx 1$ in our model. Therefore, we shall consider $c < 1$.

At $t=0$ we aim to excite the longitudinally fundamental mode of standing TAW, but we want to exclude other wave modes to be present initially. To this end, we consider an initial velocity field that is purely perpendicular to the magnetic field lines, since any perturbation parallel to the magnetic field would also excite slow MHD waves. We assume

$$v_r = 0, \quad (4)$$

$$v_\varphi = v_\perp \frac{B_z}{B}, \quad (5)$$

$$v_z = -v_\perp \frac{B_\varphi}{B}, \quad (6)$$

where $B = \sqrt{B_\varphi^2 + B_z^2}$ is the modulus of the magnetic field and v_\perp is the perpendicular velocity given by

$$v_\perp = v_0 A(r) \cos\left(\frac{\pi}{L}z\right), \quad (7)$$

where v_0 is the maximum velocity amplitude and the radial profile, $A(r)$, is the same as that used in Díaz-Suárez & Soler (2021). The velocity is zero at $r=0$, its maximum is located at $r \approx 0.64R$, and then it decreases as r increases. We set $v_0 = 0.1v_{A,0}$, where $v_{A,0} = B_0/\sqrt{\mu_0\rho_0}$ is the Alfvén velocity at $r=0$, with μ_0 the vacuum magnetic permeability.

We use the PLUTO code (Mignone et al. 2007, 2012) to numerically evolve the 3D nonlinear ideal MHD equations. The code setup is equivalent to that used in Díaz-Suárez & Soler (2021). The computational domain is initially discretized with a uniform mesh of 100 cells in each direction. We use adaptive mesh refinement (AMR) with five levels of refinement, so that the maximum effective resolution is 3200 cells in each direction. The refinement criterion is based on the second derivative error norm of a quantity related with the kinetic energy density. Regarding the boundary conditions, density, pressure, and the magnetic field components are fixed to their initial values while the velocity components are set to zero at all boundaries. This choice avoids unwanted problems like nonphysical energy injection from outside the domain, although reflections at the lateral boundaries may happen. However, the lateral boundaries are located sufficiently far away from the location where the important dynamics takes place and their influence on the simulations is minimal. Our aim is different from that of Díaz-Suárez & Soler (2021), where the onset of turbulence in a preexisting untwisted coronal loop was studied. Here, we investigate the formation of dense structures in an initially uniform corona with a twisted magnetic field.

3. Results

We study the evolution of density driven by the presence of TAW in the initially uniform plasma. Unless otherwise stated, we consider $c = 0.6$ in the simulations.

3.1. Formation of Overdense Threads

Figure 1 shows the temporal evolution of density in a transverse plane (top panels) and in a longitudinal plane (mid panels). To focus on the relevant dynamics, Figure 1 only shows a smaller subdomain of the complete numerical box.

The plasma is initially uniform but, as time increases, the density evolution undergoes two differentiated phases. The first phase is caused by phase mixing of the TAW and the associated ponderomotive force. The second phase is driven by the KHi triggered when the shear flows generated by phase mixing are strong enough.

Besides the density, we also have explored the behavior of the perpendicular velocity component (not shown here). Before the KHi onset, v_\perp shows the alternation of positive and negative velocities in adjacent radial positions, i.e., shear flows. This is an unequivocal signature of phase mixing (see, e.g., Heyvaerts & Priest 1983; Nocera et al. 1984; De Moortel et al. 2000; Smith et al. 2007; Díaz-Suárez & Soler 2021). The reason behind the presence of phase mixing in our model with uniform density is the magnetic field nonuniformity. According to Halberstadt & Goedbloed (1993), the line-tied Alfvén continuous spectrum is given by

$$\omega_A(r) = \frac{n\pi}{L} \frac{B_z(r)}{\sqrt{\mu_0\rho_0}}, \quad (8)$$

where n denotes the harmonic number. Even if the density is uniform, there is an Alfvén continuum owing to the radial variation of B_z (see Equation (3)). The Alfvén continuum naturally leads to the development of phase mixing.

Density perturbations are produced during the evolution of the phase-mixed TAW. These perturbations appear in the form of concentric rings in the transverse cut (top left panel of Figure 1) and as periodic converging/diverging flows in the longitudinal cut (mid left panel of Figure 1). These periodic density perturbations are caused by the ponderomotive force, which is a well-known nonlinear effect that couples Alfvén waves with slow MHD waves (e.g., Hollweg 1971; Rankin et al. 1994; Tikhonchuk et al. 1995; Terradas & Ofman 2004). For phase-mixed TAW, the longitudinal flows by the ponderomotive force also get out of phase as time increases (Díaz-Suárez & Soler 2021). The development of density perturbations intensifies with the triggering of the KHi owing to the shear flows associated with phase mixing (Heyvaerts & Priest 1983; Browning & Priest 1984). Unlike in Díaz-Suárez & Soler (2021), where the KHi rolls are 2D structures formed in planes perpendicular to the straight magnetic field, here the KHi rolls are 3D structures because of twist (see, e.g., Howson et al. 2017; Terradas et al. 2018).

The KHi evolves nonlinearly and develops secondary instabilities that further mix and compress the plasma (see the bottom panel of Figure 1). During the evolution of the simulation, we found overdensities of $\sim 10\%$ the initial background density. To study the 3D shape of the overdense structures, Figure 2 shows isosurfaces of the density for a value corresponding to $\sim 5\%$ enhancement. No such density enhancements are initially found, as expected. Periodic

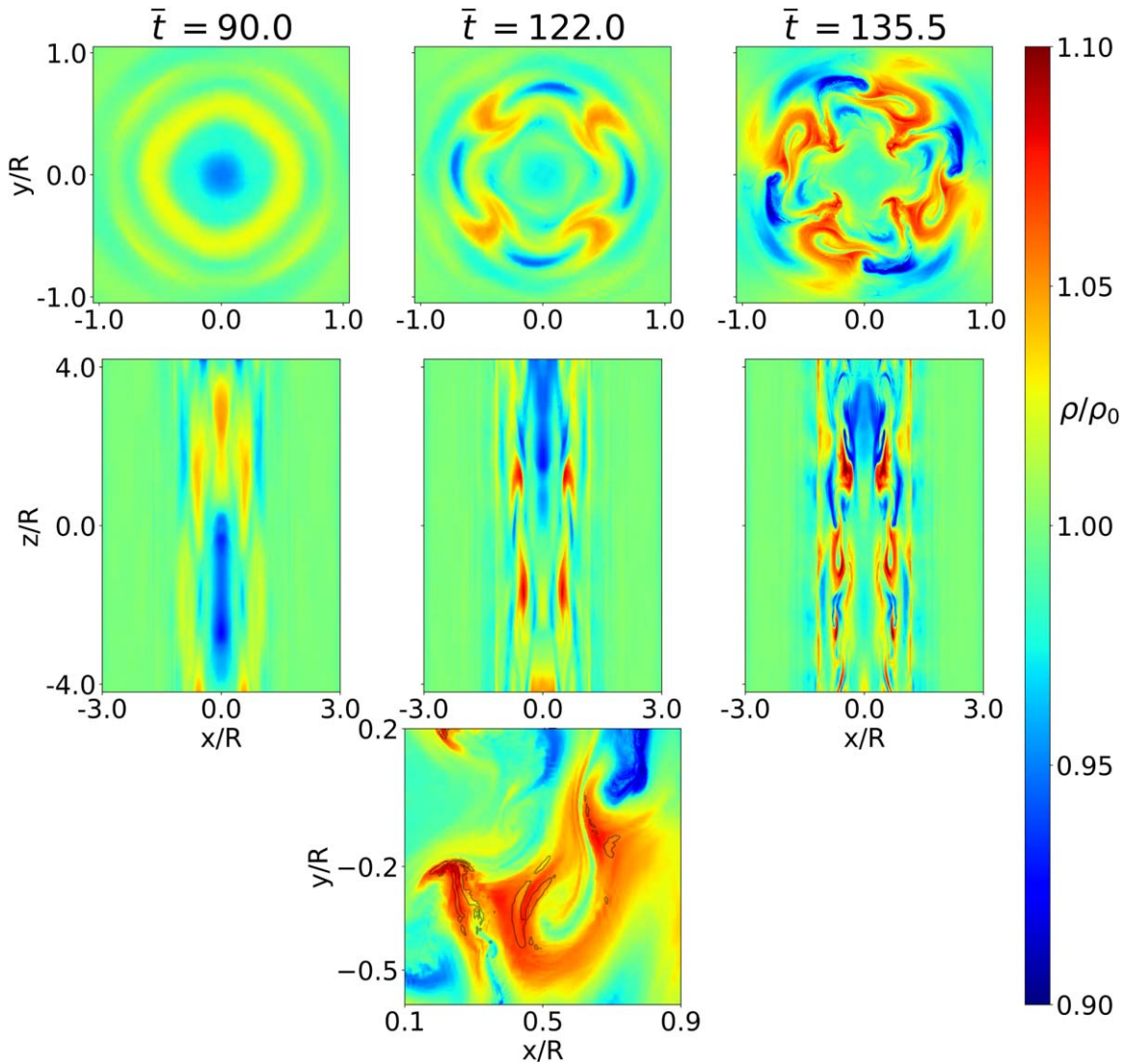


Figure 1. Top: cross-sectional cut of the density at $z = 0$ for three different simulation times. Middle: longitudinal cut of the density at $y = 0$ for the same times as before. Bottom: close-up view of a small area in the top right panel, depicting secondary instabilities and the cross-sectional shape of an overdense structure. The gray contours enclose an increase of temperature equal to or greater than 5%. Time is normalized as $\bar{t} = t v_{A,0}/R$. The snapshots are adapted from the online animation attached to this figure. The duration of the video is 15 s and shows the full temporal evolution from $\bar{t} = 0$ to 135.5.

(An animation of this figure is available.)

enhancements show up during the phase dominated by phase mixing because of the compression driven by the ponderomotive force, but no persistent structures are formed. Overdense structures are formed after the KHI develops at later times. These structures appear as elongated filaments that follow the local direction of the twisted magnetic field. At the end of the simulation, fully formed long and thin threads that outline the magnetic field structure are observed. The high-resolution AMR scheme is crucial to correctly capture the formation of the finest threads.

The plasma compression that drives the thread formation increases the gas pressure as well. Pressures larger than 20% the background pressure are found inside the threads. As a consequence of this, the inner parts of the threads are slightly hotter than the background, but to a large extent the plasma can be considered to remain approximately isothermal (see again the bottom panel of Figure 1).

3.2. Effect of the Amount of Twist

Magnetic twist plays a key role because it allows the development of phase mixing in the initially uniform plasma. Here, we explore the effect of the twist parameter, c . Additional simulations have been performed with different twist parameters. In principle, the larger c , the steeper the radial profile of ω_A . This should lead to the more rapid development of phase mixing and the quicker triggering of the KHI. Conversely, the larger c , the larger B_φ , which could have a stabilizing influence.

Following Díaz-Suárez & Soler (2021), to assess the KHI onset we use the vorticity squared integrated over the whole computational box, namely

$$\Omega^2(t) = \int |\nabla \times \mathbf{v}(\mathbf{r}, t)|^2 d^3\mathbf{r}. \quad (9)$$

Figure 3 shows the temporal evolution of Ω^2 for different values of c . Initially, Ω^2 increases owing to phase mixing (Guo et al. 2019; Howson et al. 2020; Díaz-Suárez & Soler 2021).

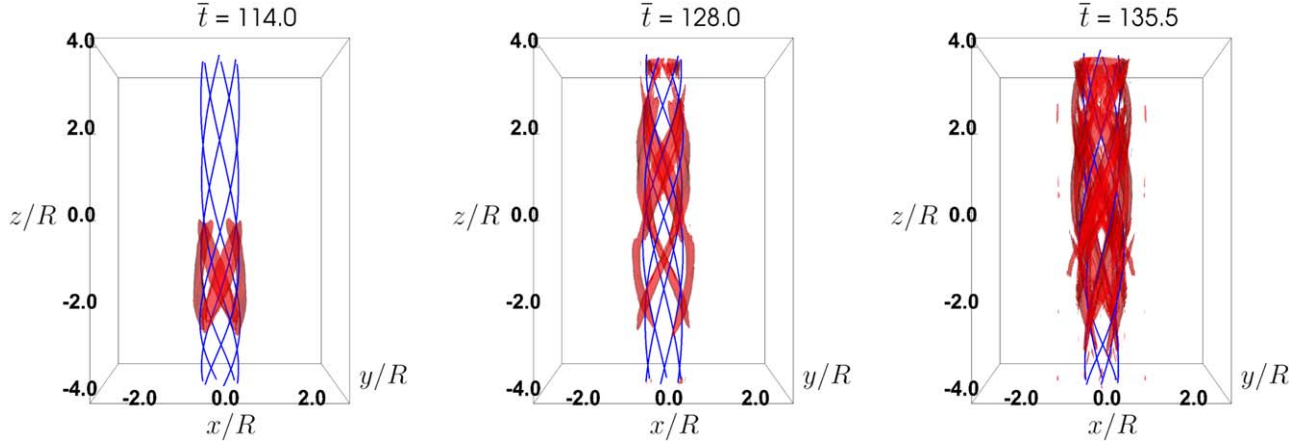


Figure 2. Density isosurfaces corresponding to 5% enhancement with respect to the background density at three different simulation times. Magnetic field lines (blue lines) located at $r/R = 0.5$ are also included. Time is normalized as $\bar{t} = t v_{A,0}/R$. The snapshots are adapted from the animation attached to this figure. The duration of the video is 15 s. The animation runs from $\bar{t} = 0$ to 135.5.

(An animation of this figure is available.)

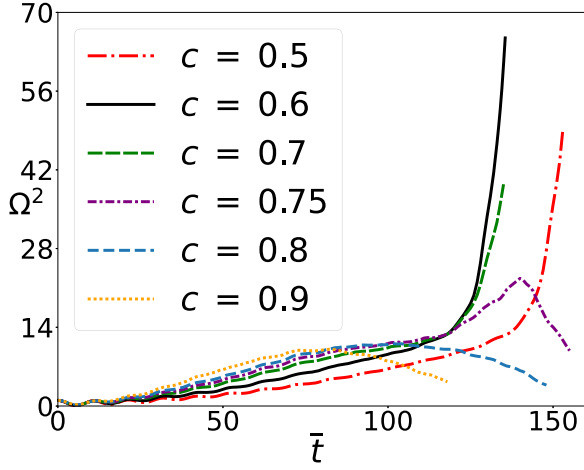


Figure 3. Vorticity squared integrated in the whole computational domain, Ω^2 , as a function of the simulation time, $\bar{t} = t v_{A,0}/R$. The different line styles correspond to different values of the twist parameter, c .

Later, two different behaviors are found depending on the twist parameter. For small and moderate twist, there is a dramatic increase in Ω^2 when the KHi is triggered and globally affects the dynamics (see Díaz-Suárez & Soler 2021). We find an earlier onset of the KHi when c increases (compare the red

dotted–dashed and black solid lines in Figure 3), being consistent with the steepening of the Alfvén continuum.

However, a different behavior is found when $c \gtrsim 0.75$. For strong twist, Ω^2 saturates and decreases at larger times. The KHi does not seem to be excited for strong twist. Detailed analysis of the simulations reveals that the KHi is actually excited, but very locally, and the perturbations are not allowed to fully grow into the nonlinear regime. Such a behavior is shown in Figure 4. The larger B_ϕ can nonlinearly avoid the instability full development. As explained in, e.g., Galinsky & Sonnerup (1994), Ryu et al. (2000), Hillier (2019) magnetic tension is responsible for nonlinearly suppressing the KHi, preventing the growth of vortices, while the shear flows developed in the system can remain linearly unstable. Nevertheless, the failed KHi is able to disrupt the phase mixing process and to stop the increase of Ω^2 . Therefore, in our model the formation of density threads via full nonlinear KHi requires weak or moderate twist.

3.3. Forward Modeling

Here, we explore what kind of observational signature the overdense threads obtained in the simulations may leave. To this end, we used the FoMo code (Van Doorselaere et al. 2016) to calculate the synthetic EUV emission for the SDO/

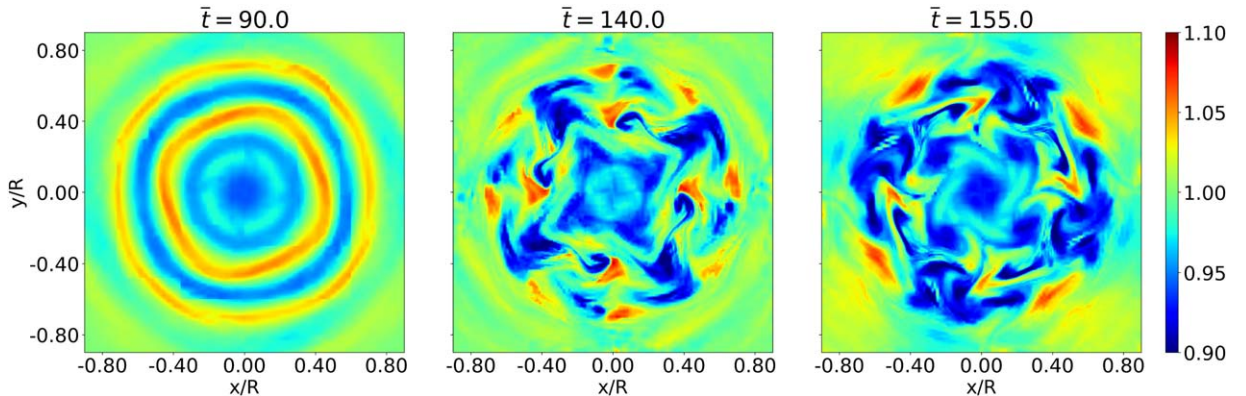


Figure 4. Cross-sectional cut of density at $z = 0$ for three different simulation times when $c = 0.75$. The left panel shows phase mixing before the KHi onset. The central panel corresponds to the time at which Ω^2 reaches its maximum (see Figure 3), the KHi is locally excited, and vortices begin to form. The right panel corresponds to a latter time, when the vortices growth has been suppressed and Ω^2 has decreased.

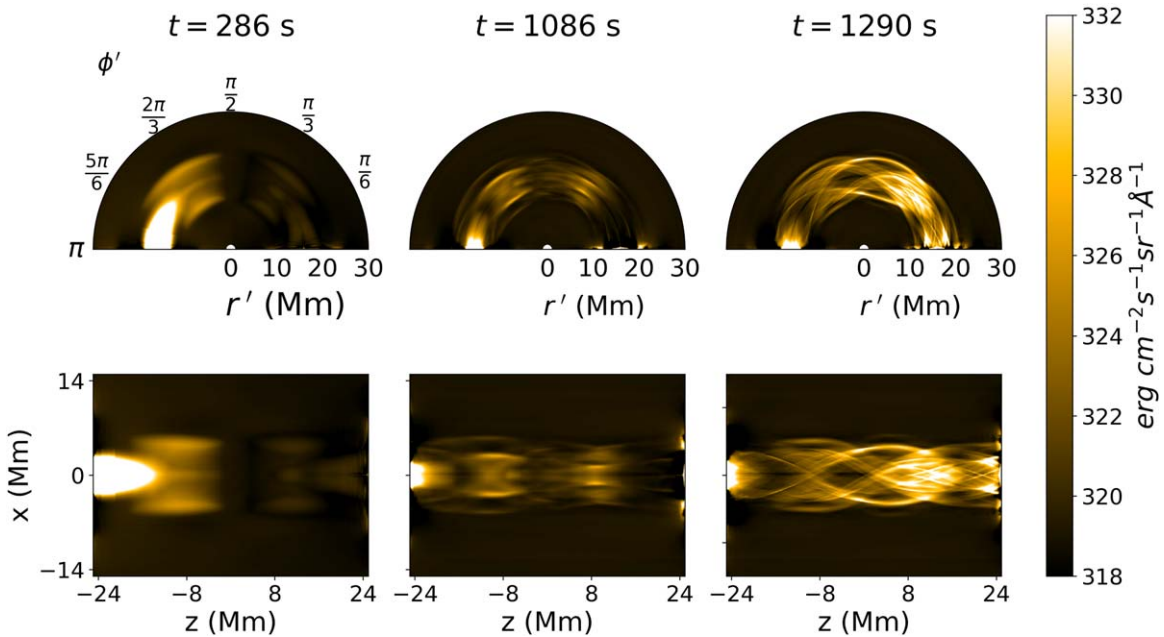


Figure 5. Synthetic SDO/AIA specific intensity at 171 \AA for three different times indicated on the top of each panel. Bottom: original simulation results. Top: transformation into a semicircular shape, with the bottom boundary representing the solar surface. The snapshots are adapted from the animation attached to this figure. The duration of the video is 15 s. The animation runs from $t = 0$ to 1290 s.

(An animation of this figure is available.)

AIA imaging telescope at 171 \AA . The FoMo code requires input data, namely velocity components, temperature, and number density, in physical units. For this application, we take $R = 5 \text{ Mm}$, $B_0 = 10 \text{ G}$, and an initial temperature of 2 MK , as typical values in the corona (see, e.g., Priest 2014). This choice results in a reference Alfvén velocity of $v_{A,0} \approx 525 \text{ km s}^{-1}$ and a number density of $\approx 2.88 \times 10^9 \text{ cm}^{-3}$ in the initially homogeneous background.

Following Van Doorselaere et al. (2016), the specific intensity along the line of sight (LOS) is computed in the FoMo code as

$$I(x'_i, y'_j) = \sum_k \kappa_\alpha(x'_i, y'_j, z'_k) \Delta l, \quad (10)$$

where κ_α is the instrument response function for a bandpass α , Δl is the resolution along the LOS, x' , y' , z' are the coordinates in a rotated frame of reference, and i, j, k are the indices in the rotated grid. The z' -direction is the LOS direction whereas x' and y' are coordinates in the plane of sky (POS). With respect to the original simulation coordinates, the LOS is set along the y -direction, while z and x are the POS coordinates.

We obtained the specific intensity by feeding the FoMo code with the results of the reference simulation with $c = 0.6$. Since actual coronal magnetic fields anchored in the photosphere are curved, we mapped the specific intensity from the original straight grid onto a semicircular grid using the transformation

$$r' = x + \frac{L}{\pi}, \quad (11)$$

$$\phi' = \left(\frac{L}{2} - z \right) \frac{\pi}{L}. \quad (12)$$

Figure 5 shows the specific intensity in the original and transformed POS. As expected, the initially homogeneous plasma emits radiation uniformly. Early in the evolution, weak

intensity variations appear due to the periodic plasma compression and expansion caused by the ponderomotive force. This effect drives longitudinal flows that are discernible in the intensity. Later, the KHi-induced threads become visible in the images. The threads appear as bright strands that illuminate and clearly reveal the underlying twisted magnetic structure. At the end of the simulation, the strands are about $\sim 5\%$ brighter than the background plasma. The apparent thickness of the bright strands in the intensity images ranges from $\sim 150 \text{ km}$ to $\sim 1500 \text{ km}$, approximately. The effective AMR resolution in this simulation is $\sim 10 \text{ km}$. The width of the finest strands is below the AIA $0''.6$ per pixel actual resolution (Lemen et al. 2012), but the thickest structures should be observable. The final simulation frame corresponds to a dimensional time of ~ 20 minute after $t = 0$.

Similar results are obtained for other AIA filters (not shown here), although the magnitude of the intensity variations and the apparent thickness of the strands may depend on the particular filter considered.

4. Discussion

In this Letter we report the results of 3D ideal MHD numerical simulations of standing TAW in a uniform plasma permeated by a line-tied magnetic field. Even with a uniform density, an Alfvén continuum is present because of the nonuniformity of the magnetic field that in our model is caused by twist, but magnetic expansion should have a similar effect (see Howson et al. 2019). The nonlinear evolution of phase mixing and the associated KHi break the uniformity of density, generating overdense structures in the form of elongated threads. These fine structures are locally aligned with the magnetic field direction. Forward modeling of SDO/AIA imaging indicates that the formed threads could appear in

observations as bright strands that illuminate the underlying coronal magnetic field.

The nonlinear evolution of TAW shares several features with that of kink MHD waves explored in the previous literature. The detailed studies of Antolin et al. (2014, 2015, 2016, 2017) on kink oscillations of a preexisting denser tube embedded in a lighter environment show how KHi-induced rolls deform the cross-sectional area of the tube and mix the internal and external plasmas at the tube boundary. This dynamics produces strand-like structures in EUV intensity images as a result of complex plasma mixing of the rolls and their appearance depends on the LOS angle. The apparent strands last for timescales of a period of the kink oscillation (Antolin et al. 2014). The apparent strands produced during kink oscillations and the TAW-induced threads reported here share a common basic mechanism, i.e., the KHi, but this Letter introduces a new process. TAW do not require a preexisting tube, density enhancement, or waveguide. In a sense, TAW represent more fundamental oscillations of the magnetic structure. The threads obtained in the present simulations are actual density structures formed in an initially uniform plasma. We demonstrate that TAW evolving in a uniform corona are able to spontaneously generate field-aligned density enhancements that may further influence the structure and dynamics of the coronal medium.

We find that the threads are $\sim 10\%$ denser than the background plasma, while the whole medium remains isothermal to a large extent. While 10% could be considered a small enhancement, it may importantly affect the subsequent evolution of the medium. The thermodynamic state in the corona is determined by a delicate balance between radiation losses, thermal conduction, and the unknown heating. Under the optically thin approximation, radiation losses in the coronal plasma are proportional to $\sim \rho^2$, so that a 10% density increase would result in about $\sim 20\%$ increase of energy losses. Equivalently, radiation losses should decrease in the regions where the density is depleted. If the background heating remains the same, the thread formation may evolve toward a situation of local thermal imbalance. We speculate that the overdense threads could behave as potential seeds of thermal instability, which is an essential ingredient of the coronal dynamics (see, e.g., Antolin 2020). This should be confirmed with nonideal simulations including thermal effects.

Finally, although we perform the simulations in a low- β scenario, the specific value of the plasma β might influence the strength of the KHi-driven compression that produces the overdense threads. A detailed analysis and parameter study of the role of the plasma β is needed. That is beyond the aim of this Letter and is left for forthcoming works.

We thank Tom Van Doorselaere for his assistance with the FoMo code. This publication is part of the R + D + i project PID2020-112791GB-I00, financed by MCIN/AEI/10.13039/

501100011033. S.D. acknowledges the fellowship PRE2018-084223 from MCIN/AEI/10.13039/501100011033 and FSE.

ORCID iDs

Sergio Díaz-Suárez  <https://orcid.org/0000-0001-8430-7314>
Roberto Soler  <https://orcid.org/0000-0001-6121-7375>

References

- Alfvén, H. 1942, *Natur*, **150**, 405
 Antolin, P. 2020, *PPCF*, **62**, 014016
 Antolin, P., De Moortel, I., Van Doorselaere, T., & Yokoyama, T. 2016, *ApJL*, **830**, L22
 Antolin, P., De Moortel, I., Van Doorselaere, T., & Yokoyama, T. 2017, *ApJ*, **836**, 219
 Antolin, P., Okamoto, T. J., De Pontieu, B., et al. 2015, *ApJ*, **809**, 72
 Antolin, P., Yokoyama, T., & Van Doorselaere, T. 2014, *ApJL*, **787**, L22
 Aschwanden, M. J., & Wang, T. 2020, *ApJ*, **891**, 99
 Browning, P. K., & Priest, E. R. 1984, *A&A*, **131**, 283
 De Moortel, I., Hood, A. W., & Arber, T. D. 2000, *A&A*, **354**, 334
 De Pontieu, B., Carlsson, M., Rouppe van der Voort, L. H. M., et al. 2012, *ApJL*, **752**, L12
 Díaz-Suárez, S., & Soler, R. 2021, *A&A*, **648**, A22
 Galinsky, V. L., & Sonnerup, B. U. Ö 1994, *GeoRL*, **21**, 2247
 Gold, T., & Hoyle, F. 1960, *MNRAS*, **120**, 89
 Guo, M., Van Doorselaere, T., Karamelas, K., et al. 2019, *ApJ*, **870**, 55
 Halberstadt, G., & Goedbloed, J. P. 1993, *A&A*, **280**, 647
 Heyvaerts, J., & Priest, E. R. 1983, *A&A*, **117**, 220
 Hillier, A. 2019, *PhPI*, **26**, 082902
 Hollweg, J. V. 1971, *JGR*, **76**, 5155
 Hood, A. W., & Priest, E. R. 1979, *SoPh*, **64**, 303
 Howson, T. A., De Moortel, I., & Antolin, P. 2017, *A&A*, **607**, A77
 Howson, T. A., De Moortel, I., Antolin, P., Van Doorselaere, T., & Wright, A. N. 2019, *A&A*, **631**, A105
 Howson, T. A., De Moortel, I., & Reid, J. 2020, *A&A*, **636**, A40
 Jess, D. B., Mathioudakis, M., Erdélyi, R., et al. 2009, *Sci*, **323**, 1582
 Karamelas, K., Van Doorselaere, T., & Antolin, P. 2017, *A&A*, **604**, A130
 Kohutova, P., Verwichte, E., & Froment, C. 2020, *A&A*, **633**, L6
 Lemen, J. R., Title, A. M., Akin, D. J., et al. 2012, *SoPh*, **275**, 17
 Magyar, N., & Van Doorselaere, T. 2016, *A&A*, **595**, A81
 Mignone, A., Bodo, G., Massaglia, S., et al. 2007, *ApJS*, **170**, 228
 Mignone, A., Zanni, C., Tzeferacos, P., et al. 2012, *ApJS*, **198**, 7
 Nocera, L., Priest, E. R., & Leroy, B. 1984, *A&A*, **133**, 387
 Pagano, P., De Moortel, I., & Morton, R. J. 2020, *A&A*, **643**, A73
 Priest, E. 2014, *Magnetohydrodynamics of the Sun* (Cambridge: Cambridge Univ. Press)
 Rankin, R., Frycz, P., Tikhonchuk, V. T., & Samson, J. C. 1994, *JGR*, **99**, 21291
 Ryu, D., Jones, T. W., & Frank, A. 2000, *ApJ*, **545**, 475
 Smith, P. D., Tsiklauri, D., & Ruderman, M. S. 2007, *A&A*, **475**, 1111
 Soler, R., Terradas, J., Oliver, R., & Ballester, J. L. 2019, *ApJ*, **871**, 3
 Soler, R., Terradas, J., Oliver, R., & Ballester, J. L. 2021, *ApJ*, **909**, 190
 Spruit, H. C. 1982, *SoPh*, **75**, 3
 Terradas, J., Andries, J., Goossens, M., et al. 2008, *ApJL*, **687**, L115
 Terradas, J., Magyar, N., & Van Doorselaere, T. 2018, *ApJ*, **853**, 35
 Terradas, J., & Ofman, L. 2004, *ApJ*, **610**, 523
 Tikhonchuk, V. T., Rankin, R., Frycz, P., & Samson, J. C. 1995, *PhPI*, **2**, 501
 Van Doorselaere, T., Antolin, P., Yuan, D., Reznikova, V., & Magyar, N. 2016, *FRASS*, **3**, 4